




Article

Influence of Anodizing by Electro-Chemical Oxidation on Fatigue and Wear Resistance of the EV31A-T6 Cast Magnesium Alloy

Gianluca Di Egidio ^{1,*}, Lavinia Tonelli ¹, Alessandro Morri ¹, Iuri Boromei ¹, Pavel Shashkov ² and Carla Martini ¹

¹ Department of Industrial Engineering (DIN), Alma Mater Studiorum, University of Bologna, Viale Risorgimento 4, 40136 Bologna, Italy

² Cambridge Nanolitic Ltd., 3b Homefield Road, Haverhill, Suffolk CB9 8QP, UK

* Correspondence: gianluca.diegido2@unibo.it

Abstract: In the last decades, several anodizing processes for Mg alloys have been proposed to achieve a good wear and corrosion resistance combination. In particular, Electro-Chemical Oxidation (ECO) showed an improved dense and compact anodized layer compared to other anodizing processes carried out above the dielectric breakdown voltage, such as Plasma Electrolytic Oxidation (PEO). However, the influence of the ECO treatment on the tribological behavior and cyclic mechanical performance of Mg alloys has not been investigated yet. This paper reports on the influence of ECO on dry sliding behavior (vs. 100Cr6 bearing steel (block-on-ring contact geometry)) and rotating bending fatigue performance of the rare earth (RE)-containing Mg alloy EV31A-T6, comparing it with both untreated EV31A-T6 and PEO-treated EV31A-T6, used as benchmarks. The ECO-treated alloy showed improved tribological behavior (critical load for coating failure one order of magnitude higher and coefficient of friction 40% lower than for PEO) and fatigue strength (no decrease for ECO-treated samples compared to the untreated alloy, while PEO-treated samples induced a 15% decrease) due to the increased compactness and lower defectivity of the anodized layer, induced by the minimization of destructive arc discharges during coating growth. In addition, the ECO treatment significantly improved wear resistance compared to the untreated alloy, avoiding, at the same time, the decrease in fatigue strength, which typically occurs after PEO. Therefore, the ECO process can be applied to improve wear resistance without decreasing the fatigue strength of high-performance components.

Keywords: rare earth magnesium alloy; electro chemical oxidation; plasma electrolytic oxidation; microstructure; fatigue strength; dry sliding; wear resistance



Citation: Di Egidio, G.; Tonelli, L.; Morri, A.; Boromei, I.; Shashkov, P.; Martini, C. Influence of Anodizing by Electro-Chemical Oxidation on Fatigue and Wear Resistance of the EV31A-T6 Cast Magnesium Alloy. *Coatings* **2023**, *13*, 62. <https://doi.org/10.3390/coatings13010062>

Academic Editor: Matjaž Finšgar

Received: 8 December 2022

Revised: 26 December 2022

Accepted: 28 December 2022

Published: 29 December 2022



Copyright: © 2022 by the authors. Licensee MDPI, Basel, Switzerland. This article is an open access article distributed under the terms and conditions of the Creative Commons Attribution (CC BY) license (<https://creativecommons.org/licenses/by/4.0/>).

1. Introduction

Mg alloys are increasingly used as lightweight materials in the aerospace and automotive industries due to their high specific strength, damping ability, and good castability [1]. The addition of Rare Earth (RE) elements has been demonstrated to improve the tensile and fatigue strength of Mg alloys due to both microstructural refinement and the decrease of solidification defects in cast alloys [2–4], as well as the reduction of twinning in wrought Mg alloys [5–8]. Furthermore, the introduction of RE can improve corrosion resistance in combination with the reduction of impurities in the alloy [9]; in particular, Neodymium (Nd) and Gadolinium (Gd) contribute to improving surface passivity and suppressing galvanic micro-couples [10]. These alloy additions also improve the precipitation hardening response and reduce production costs [11].

Among RE-containing Mg alloys, EV31A (also known as Elektron 21[®], with Nd and Gd up to 3.1 and 1.7 wt.%, respectively, [12]) has been proposed for automotive/motorsport components such as steering system elements, camshaft covers, clutch and transmission housings, frame elements, and wheels, which may be subjected to sliding or cyclic stresses

in service. Several surface modifications have been proposed for Mg alloys to achieve a good combination of wear and corrosion resistance [13–15]. Among them, anodizing above the oxide breakdown voltage (often termed either Plasma Electrolytic Oxidation (PEO) or Micro-Arc Oxidation (MAO)) has gained increasing research interest in the last couple of decades. These electro-chemical conversion treatments are based on modifying the growing anodic layer by micro spark/arc discharges to enhance its thickness and hardness. The latter can be further increased by involving species from the electrolyte and thus forming out-of-equilibrium phases. Careful control of the discharge regime is required to avoid the onset of destructive discharges, which may detrimentally affect the quality of the anodized layer [16–18].

However, anodizing (both above or below the oxide breakdown voltage) is known to detrimentally affect fatigue behavior, primarily due to oxidation-induced surface tensile stress, structural defects in the anodic oxide, and age softening of the substrate, as well as to heating during oxide film formation [19]. The influence of PEO on fatigue has been mainly investigated for conventional Mg alloys without RE additions [20,21], showing that the fatigue limit reduction induced by PEO ranged from about 10% [19] to 37% [22].

From a tribological point of view, even though PEO remarkably improves wear resistance, the high roughness in the as-treated condition may generate relatively high friction against steel counterparts in dry sliding conditions [23].

In order to improve the overall mechanical performance, defects in the anodic oxide may require sealing post-treatments [24,25], making the production cycle more time-consuming and less cost-effective.

An enhanced anodizing process called ECO (Electro Chemical Oxidation) has been recently developed (UK Patent GB2497063, Cambridge Nanolitic Ltd.) to overcome these drawbacks. ECO derives from PEO but uses bipolar pulsed DC sources to avoid disruptive plasma discharge effects and provide dense and compact coatings. The formation of a finer nanopore structure oxide layer was promoted by: (i) using short (microseconds) electrical pulses with trapezoidal shape to reduce the electrical current peaks during pulse switching; (ii) maintaining cathodic current at a level that secures cathodic etching; (iii) avoiding breakdown discharge and improve ion and charge transfer to the oxidation zone. ECO coatings have already been applied in the textile, packaging, and automotive industries. In particular, a previous study on the wrought AA6082-T5 alloy demonstrated that ECO improves tribological behavior compared to PEO [26]. However, the influence of ECO on the tribological and fatigue behavior of Mg alloys has not been investigated yet. In this work, the conditions for ECO treatment (carried out in pulsed bipolar current) differ from those applied in another recent paper [27] dealing with galvanostatic anodizing of AZ31B. We also reported on the tribological behavior of ECO-treated samples, which is not covered in the above-cited reference. Based on the above, the present study investigates the influence of ECO on dry sliding and rotating bending fatigue behavior of the RE-containing Mg alloy EV31A using data from previous studies on tribological [28] and fatigue [29] performance of PEO-treated EV31A as a benchmark.

2. Materials and Methods

The Mg alloy EV31A (chemical composition in Table 1) was provided by Magnesium Elektron Ltd. (Manchester, UK). Blocks for dry sliding tests ($5 \times 5 \times 70 \text{ mm}^3$) and rotating bending fatigue test samples (smooth cylindrical specimen geometry according to ISO 1143 [30]) were machined from sand-cast plates. All samples were heat treated (T6) by (i) solutionizing at $520 \text{ }^\circ\text{C}$ for 8 h, (ii) quenching in $70 \text{ }^\circ\text{C}$ water, and (iii) aging at $200 \text{ }^\circ\text{C}$ for 16 h [31].

Table 1. Chemical composition (wt.%) of the EV31A Mg alloy.

Nd	Gd	Zr	Zn	Fe	Ni	Cu	Si	Ag	ORE ¹	Mg
2.8	1.3	0.56	0.29	0.003	<0.001	<0.008	<0.01	<0.1	<0.14	Bal.

¹ ORE = Other Rare Earths, i.e., Ce, La, Pr.

Before Electro-Chemical Oxidation (ECO) and Plasma Electrolytic Oxidation (PEO), EV31A samples were polished by standard metallographic techniques and degreased in ultrasonicated acetone.

The main treatment parameters for ECO, which was carried out in an industrial environment, are listed in Table 2 and compared to those for the PEO treatments used as benchmarks for tribological and fatigue tests. The PEO benchmark for dry sliding tests (“PEO-tribo”) was carried out on the lab scale, while the PEO benchmark for fatigue tests (“PEO-fatigue”) was carried out on the industrial scale by a proprietary process (MAGOXID®) [29]. This paper reports complete data regarding the microstructure, tribological, and fatigue behavior of ECO-treated EV31A. Basic information on PEO benchmarks is reported only for comparison (Table 3). The corresponding studies are detailed in [28] for PEO-tribo and in [29] for PEO-fatigue.

Table 2. Main features of the anodizing treatments.

Anodizing Parameters	ECO	PEO-Tribo [28]	PEO-Fatigue [29]
Coating mode control	Pulsed bipolar current (PBC): Potentiostatic for anodic pulse; galvanostatic for cathodic pulses	Galvanostatic (DC mode)	
Voltage (V)	+500 V / −100 V	<200 V	
Current density (mA cm ^{−2})	600	500	MAGOXID® (proprietary process)
Electrolyte	Alkaline phosphate-aluminate solution (KOH, Na ₄ O ₇ P ₂ , NaAlO ₂ in deionized water)	Alkaline phosphate-silicate solution (Na ₅ P ₃ O ₁₀ , Na ₂ SiO ₃ , NaOH in deionized water)	
Tank temperature (°C)	20–25	20–25	
Discharge mode	Low-discharge oxidation	Micro-discharge oxidation	Micro-discharge oxidation

Table 3. Main features of the ECO layers and PEO benchmarks investigated by tribological (dry sliding) and fatigue (4-point rotating bending, staircase method) tests. Results on benchmarks come from our previous studies on the tribological [28] and fatigue [29] behavior of PEO-treated EV31A-T6.

Main Coating Features, Tribological and Fatigue Properties	Dry Sliding				Rotating Bending			
	ECO-Tribo		PEO-Tribo [28]		ECO-Fatigue		PEO-Fatigue [29]	
	R _a	R _q	R _a	R _q	R _a	R _q	R _a	R _q
Surface roughness, μm	0.19 ± 0.04	0.24 ± 0.04	5.3 ± 0.8	6.9 ± 2.0	0.30 ± 0.02	0.38 ± 0.02	2.0 ± 0.1	2.4 ± 0.3
Thickness, μm	55 ± 6		47 ± 10		16 ± 4		23 ± 3	
Phase constitution	MgO		MgO, Mg ₃ (PO ₄) ₂ , Mg ₂ SiO ₄		MgO		MgO, Mg ₃ (PO ₄) ₂ , Mg ₂ P ₂ O ₇	
L _{c3} (scratch test), N	>30		21.7 ± 2.6		21.1 ± 2.0		13.3 ± 0.6	
Maximum load before coating failure (dry sliding), N	50		5		n.a.		n.a.	
Mean fatigue strength (σ _{D[50%]}), MPa	n.a.		n.a.		109 ± 5 (no decrease in comparison to untreated alloy)		88 ± 13 (−15% in comparison to untreated alloy)	

n.a.: not applicable.

After ECO, samples for tribological tests were gently rubbed with an abrasive pad (3M Scotch-Brite hand pad) to remove the thin powdery top layer and then rinsed again with demineralized water. Samples for fatigue tests were only rinsed with demineralized water after ECO.

2.1. Microstructural Characterization

Microstructural characterization of untreated EV31A-T6 was carried out by standard metallographic techniques, using Nital 2 (2 mL HNO₃, 98 mL EtOH) to highlight the microstructure. Optical microscopy (Reichert MeF3, Depew, NY, USA) and Field Emission Gun Scanning Electron Microscopy (FEG-SEM Tescan Mira 3, Brno, Czech Republic) equipped with Energy Dispersive Spectroscopy (EDS) microprobe (Bruker XFlash 630M, Billerica, MA, USA) were used for microstructural observations. Thickness measurements were carried out on cross section images of anodic oxides using the ImageJ software by averaging data obtained by at least 5 measurements at the same magnification. The phase constitution of the PEO layers was determined by X-ray diffraction (XRD), performing θ - 2θ scans from 10° to 100° with a 0.02 step size and a 4 s dwell time by a PANalytical X'pert PRO (Malvern, UK) X-ray diffractometer with Xcelerator detector and a Ni-filtered Cu-K α radiation source ($\lambda = 0.15405$ nm), operated at 40 kV and 30 mA. Topographic measurements were carried out on free-coating surfaces by stylus profilometry (Homelwerke T2000, Schweningen, Germany, radius of curvature of the stylus tip: 5 μ m). Microhardness vs. depth profiles was measured on polished cross-sections using a Knoop microhardness tester with a load of 100 g (HK_{0.1}). In addition, Vickers micro-hardness (HK_{0.1}) was measured on free surfaces. Scratch tests were performed using a Revetest device (CSM Instruments SA, Peseux, Switzerland) equipped with a Rockwell diamond indenter (spherical tip radius: 200 μ m). Progressive load scratch tests were conducted from 1 to 30 N, with a linear speed rate of 10 mm min⁻¹ and a scratch length of 10 mm. Scratches morphology was observed by optical microscopy during scratching and by 3-D digital microscopy and SEM after testing.

2.2. Tribological Tests

Dry sliding tests were carried out on untreated EV31A-T6 and the anodized alloy using a flat-on-cylinder tribometer (block-on-ring contact geometry, ASTM G-77 [32]). Stationary samples (5 × 15 × 70 mm³) slide against a rotating 100Cr6 (AISI 52100) bearing steel cylinder (diameter: 40 mm), with a surface hardness of 60 HRC and a roughness Ra = 0.15 ± 0.03 μ m. Tests were performed at ambient temperature and humidity (relative humidity ranging from 50 to 60%), at fixed sliding speed (0.3 m s⁻¹), under normal loads from 5 to 60 N and 1000 m sliding distance. These conditions led to maximum Hertzian contact pressures ranging from 40 to 150 MPa, estimated according to [33], considering MgO as the prevalent phase in anodic oxides (elastic modulus E = 248 GPa and Poisson's ratio $\nu = 0.187$ [34]), as determined by XRD analysis. Friction force values were continuously recorded during each test as a function of sliding distance by a bending load cell. Friction values were averaged over the steady-state regime for each test and then averaged again over each test's repetitions. Linear vertical displacement of both mating bodies (i.e., slider + cylinder) was monitored during the tests by LVDT, while the maximum wear scar depth was separately measured at the end of each test on sliders and cylinders by stylus profilometry (tip radius: 5 μ m). Worn surfaces were characterized by Hirox KH 7700 (Tokio, Japan) 3D-digital microscope and FEG-SEM/EDS to identify the dominant wear mechanisms.

2.3. Fatigue Tests

Rotating bending fatigue tests were carried out by adopting a 4-point loading configuration at a frequency of 90 Hz and a stress ratio R = -1 on ECO-treated cylindrical samples [30]. Tests were performed following the statistical staircase method, described in ISO 12107 [35], in which specimens are tested sequentially under increasing stresses until a failure occurs. The tests start at a first stress level, preferably close to the estimated mean strength, to find if samples fail before the given number of cycles or not. The fatigue strength with a 50% survival probability was assessed with a maximum number of cycles of 2 × 10⁶ cycles and a stress step of 5 MPa. These conditions led to a test duration of about 6.5 h for each run-out test. The investigated load ranged from 100 to 125 MPa, and tests

at each load step were repeated up to 4 times. FEG-SEM analyses of the fracture surfaces were performed to identify the failure mechanisms.

3. Results

3.1. Microstructural Characterization

Figure 1 shows the microstructure of the EV31A cast alloy after T6 heat treatment, where typical needle-like Zr-Zn clusters were observed at the grain core. In this alloy, Zr addition contributes to grain refining, while Zn beneficially affects mechanical properties and mitigates adverse effects of Fe and Ni impurities on corrosion behavior [36]. Residual eutectic microconstituent (α -Mg + $Mg_{12}Nd_xGd_{(1-x)}$) was detected at grain boundaries (Figure 1b), as also reported in [28,37].

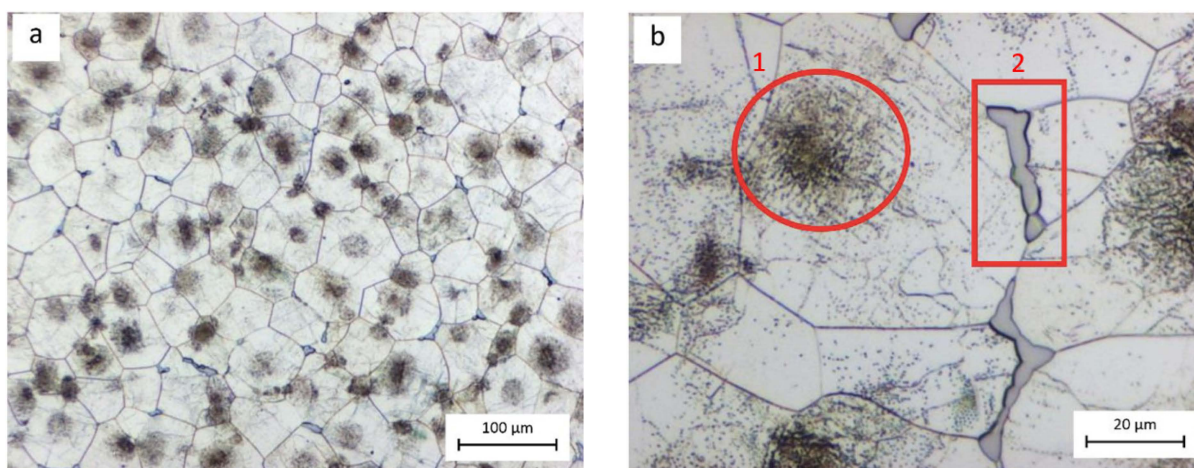


Figure 1. Microstructure of the cast EV31A-T6 Mg alloy after etching with Nital 2 [38]: general view (a) and high-magnification detail (b) showing Zr-Zn clusters at grain core (1) and residual eutectic microconstituent (α -Mg + $Mg_{12}Nd_xGd_{(1-x)}$) at grain boundaries (2).

Figure 2 compares the free surface morphology of PEO- and ECO-treated EV31A. Shallow grooves on the surface of flat sliders for tribological tests (Figure 2b,c) are due to the light rubbing procedure carried out to remove the thin powdery top layer, as described in Section 2. However, both tribological and fatigue samples (unaltered after treatment, Figure 2e,f) show typical craters generated by local discharge events occurring during the anodic oxide growth. Pancake morphology, due to molten oxide ejected from discharge channels and rapidly cooled, as well as a few microcracks due to thermal stresses, were also observed. However, the low intensity of micro-discharges in ECO induced a rather fine surface morphology, as indicated by lower roughness values than PEO (Table 3) and the images in Figure 2 (a vs. b; d vs. e).

Cross-section backscattered electron (BSE) images of the ECO layers are shown in Figure 3 and compared with the corresponding PEO layers. The interface between the ECO layer and the substrate is wavy due to the local thickening of the anodic oxide due to breakdown events and the presence of Gd- and Nd-rich second-phase particles [39]. The thickness of the ECO layer on samples for fatigue tests was deliberately kept lower than for tribological tests (Table 3) to minimize detrimental effects related to the build-up of stresses and defects in the outer layer of the coating. As reported in [40], fatigue strength decreases with increasing anodized layer thickness. However, all ECO layers (Figure 3b,c,e,f) were fairly dense and displayed only a few tiny pores and discharge channels, primarily located in the outermost zone. Conversely, PEO layers (Figure 3a,d) showed many large pores and cracks, most noticeably in the tribological samples (Figure 3a). The main reason for these differences is related to less intense micro-arcs generated by the improved control of the discharge regime in the ECO process, as already observed in previous works [26].

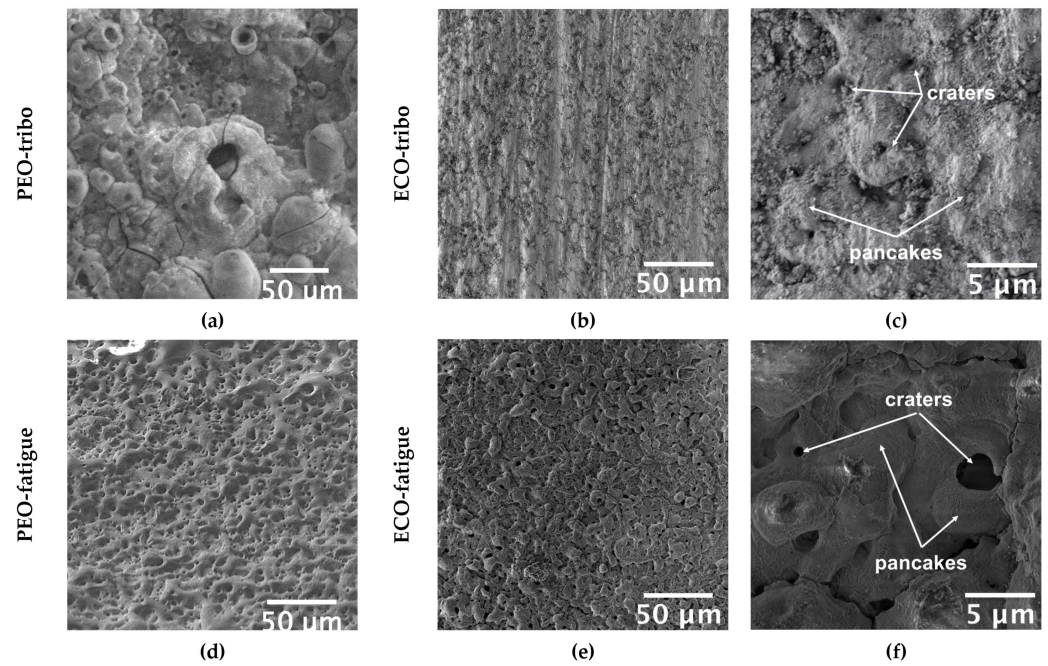


Figure 2. Surface morphology (FEG-SEM images) of the PEO (a,d) and ECO (b,c,e,f) layers on cast EV31A-T6 Mg alloy samples for tribological (a–c) and fatigue (d–f) testing. Light rubbing marks (vertical grooves) are visible in (b) due to the procedure for removing the thin powdery top layer after ECO treatment.

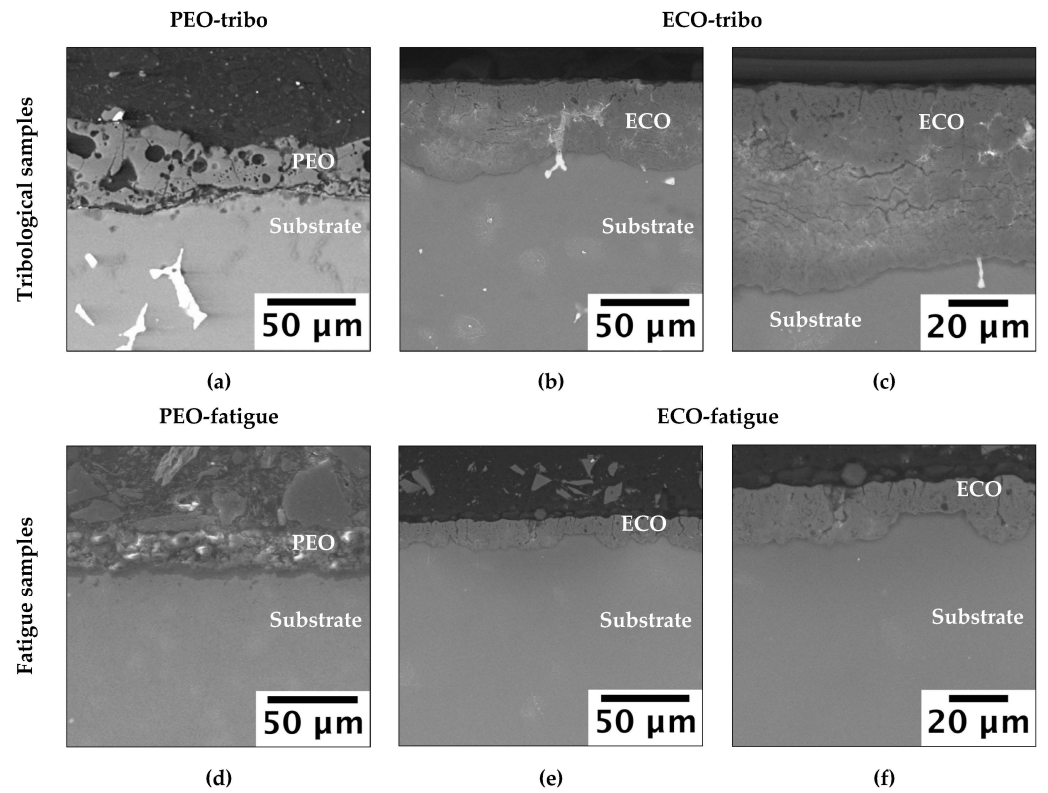


Figure 3. Polished cross sections (BSE images) of the anodic layers on cast EV31A-T6: PEO (a,d) and ECO layers (b,c,e,f) on samples for tribological (a–c) and fatigue (d–f) testing.

BSE images in Figure 3b,c and elemental X-ray maps recorded by EDS on polished cross sections (Figure 4) evidenced the incorporation of the Nd- and Gd-rich eutectic

microconstituent layer and the overall distribution of the elements in second-phase particles within the growing ECO-produced anodic oxide. RE-containing particles incorporated into the ECO layer underwent a slight volume increase due to oxidation, as also observed by Arrabal et al. [39].

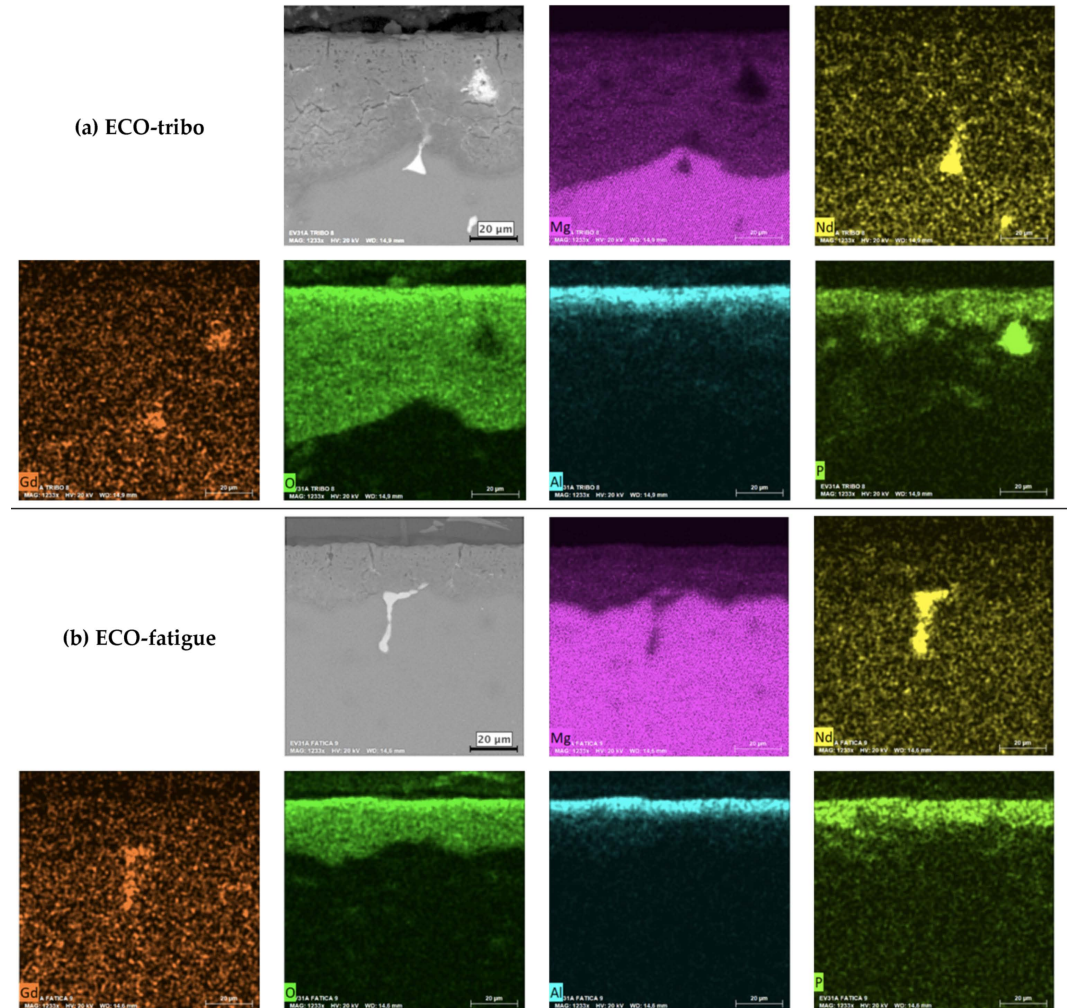


Figure 4. BSE images and EDS X-Ray maps showing elemental distribution in cross section for the ECO layer on cast EV31A-T6: tribological (ECO-tribo) (a) and fatigue (ECO-fatigue) samples (b).

Regarding elements from the electrolyte (Al and P), X-ray maps in Figure 4 show that Al-rich species were mainly located in the outer areas of the ECO layer, while P-rich species were detected at a higher depth from the surface. The distribution of these elements is influenced by the ionic mobility of the corresponding species, as discussed by Monfort et al. [41] and Matykina et al. [42].

XRD analyses (Figure 5) revealed that MgO is the main crystalline constituent of the ECO layers. Also, peaks from the Mg substrate were detected, indicating that XRD patterns represent the coating's full-thickness composition. The lower thickness of the ECO-fatigue layers led to a higher contribution from the Mg substrate than the thicker ECO-tribo layers.

Figure 6 shows a representative $HK_{0.1}$ vs. depth profile measured on the polished cross section of the ECO-tribo layer. The highest microhardness within the ECO layer (about 470 $HK_{0.1}$) was found at about 6 µm from the coating-substrate interface, close to the base material. The microhardness value decreased towards the outer surface of the layer, reaching a plateau between 230 and 210 $HK_{0.1}$ at about 30 µm from the coating-substrate interface. A similar trend was obtained by Durdu et al. [43], even though with higher microhardness values; in particular, the highest microhardness was measured in the

densest inner layer, approximately at 7 μm from the coating-substrate interface, while a decrease of about 50% was measured at 30 μm distance from it.

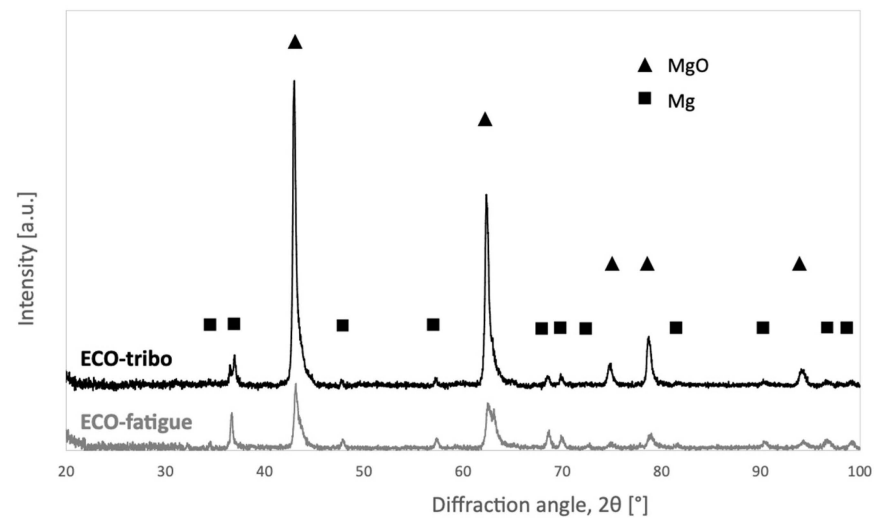


Figure 5. X-ray diffraction patterns, representative of the through-thickness composition of ECO layers on cast EV31A-T6.

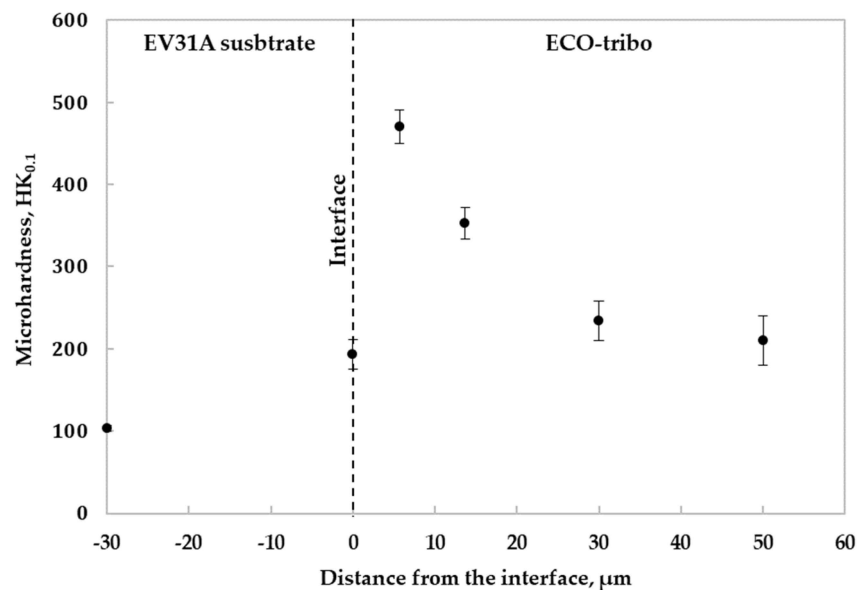


Figure 6. Cross-sectional Knoop indentation profiles of ECO layers on tribological samples (ECO-tribo).

Due to the PEO layer's lower compactness, it was impossible to measure a comparable $\text{HK}_{0.1}$ vs. depth profile. However, surface hardness values were measured on both anodic layers, confirming that ECO's dense and fine microstructure ($\text{HV}_{0.1} = 451 \pm 8$) led to a slightly higher hardness than PEO ($\text{HV}_{0.1} = 378 \pm 10$).

Scratch test results, expressed as Lc3, i.e., the critical load for full adhesive failure, according to ISO 20502 [44], are summarized in Table 3. ECO and PEO layers on EV31A can be considered hard coating on a softer substrate. These layers plastically deform as they are bent into the scratch track formed due to substrate plastic deformation under increasing normal load. Buckling failures (cracks and patches of coating spallation) progressively appear within the track, in the regions of plastic pile-up ahead of the advancing indenter. Critical loads for adhesive failure are known to be significantly influenced by the thickness and roughness of the coated surfaces [45]. Therefore, it is not surprising to observe higher Lc3 values for both the layers obtained on tribological testing samples than on fatigue

samples. However, for each type of sample, the ECO layers attain higher Lc3 than PEO due to the smoother surface (R_q always about one order of magnitude lower than for PEO, Table 3) and more compact microstructure (Figure 3).

3.2. Dry Sliding Tests

Representative plots comparing the coefficient of friction (COF) as a function of sliding distance for ECO- and PEO-treated EV31A and the untreated substrate are shown in Figure 7a.

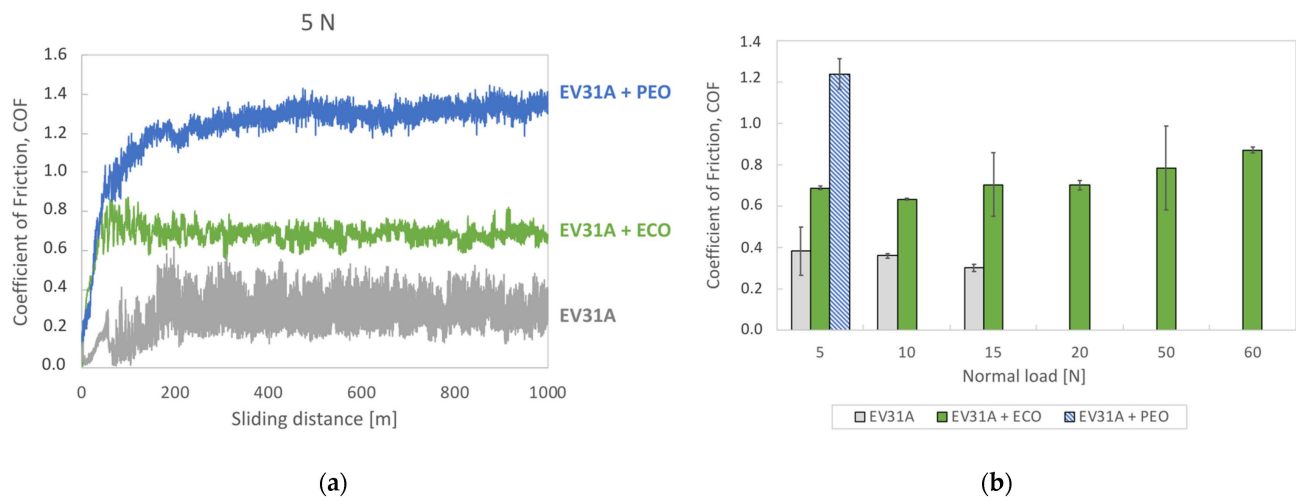


Figure 7. Dry sliding tests (vs. 100Cr6 steel, 1000 m, 0.3 m/s): dynamic COF as a function of sliding distance for untreated and ECO-treated EV31A at 5 N, compared to PEO-treated EV31A [28] (a); average values of steady-state coefficient of friction for all tested conditions (data for PEO-treated EV31A at 5 N from [28]) (b).

This comparison was possible only at the lowest load (5 N) since, above 5 N, the PEO layer was utterly worn out before the end of the test. In steady-state conditions, both the ECO and the PEO treatment led to an increase of COF compared to the untreated EV31A alloy due to the increase in the abrasive component of friction, in agreement with previous findings [28,46,47]. However, the COF increase brought about by ECO is lower than by PEO (+75% instead of +200%, as shown by average steady-state COF data in Figure 7b). This result is due to the lower roughness of the ECO layer (Table 3), generated by its more compact microstructure (Figure 3), as discussed in Section 3.1. Figure 7b also shows that, for ECO layers, COF is not significantly affected by normal load. The slight COF increase with increasing normal load may be ascribed to the decreasing stability of the iron oxide-based transfer layer which forms on the surface of sliders as a consequence of mild tribo-oxidation of the steel counterpart under the combined action of mechanical stresses and frictional heating, as also observed in previous studies [28]. Figure 8 shows the accumulation onto the surface of the ECO layer of reddish transfer layers, which is facilitated by both the topography of the anodic layer (Figure 2) and the load support provided by the ECO layer itself.

The wear track coverage and the transfer layers stability on the ECO-treated surface (slider) increased with increasing normal load up to 15 N (Figure 8a,e,i). Correspondingly, the steel counterpart (cylinder) underwent mild tribo-oxidation, forming shallow grooves (Figure 8b,f,j): the wear depth on the cylinder was consistently undetectable by stylus profilometry. Conversely, the untreated substrate (Figure 8c,g,k) was unable to form/stabilize any protective transfer layer and underwent severe adhesive/abrasive wear, showing a deeply ploughed and plastically deformed bright metallic surface. The macroscopic observation of the steel counterpart showed even fewer wear damage signs than after tests vs. the ECO-treated sliders. Therefore, the wear depth on the cylinder was undetectable in this case.

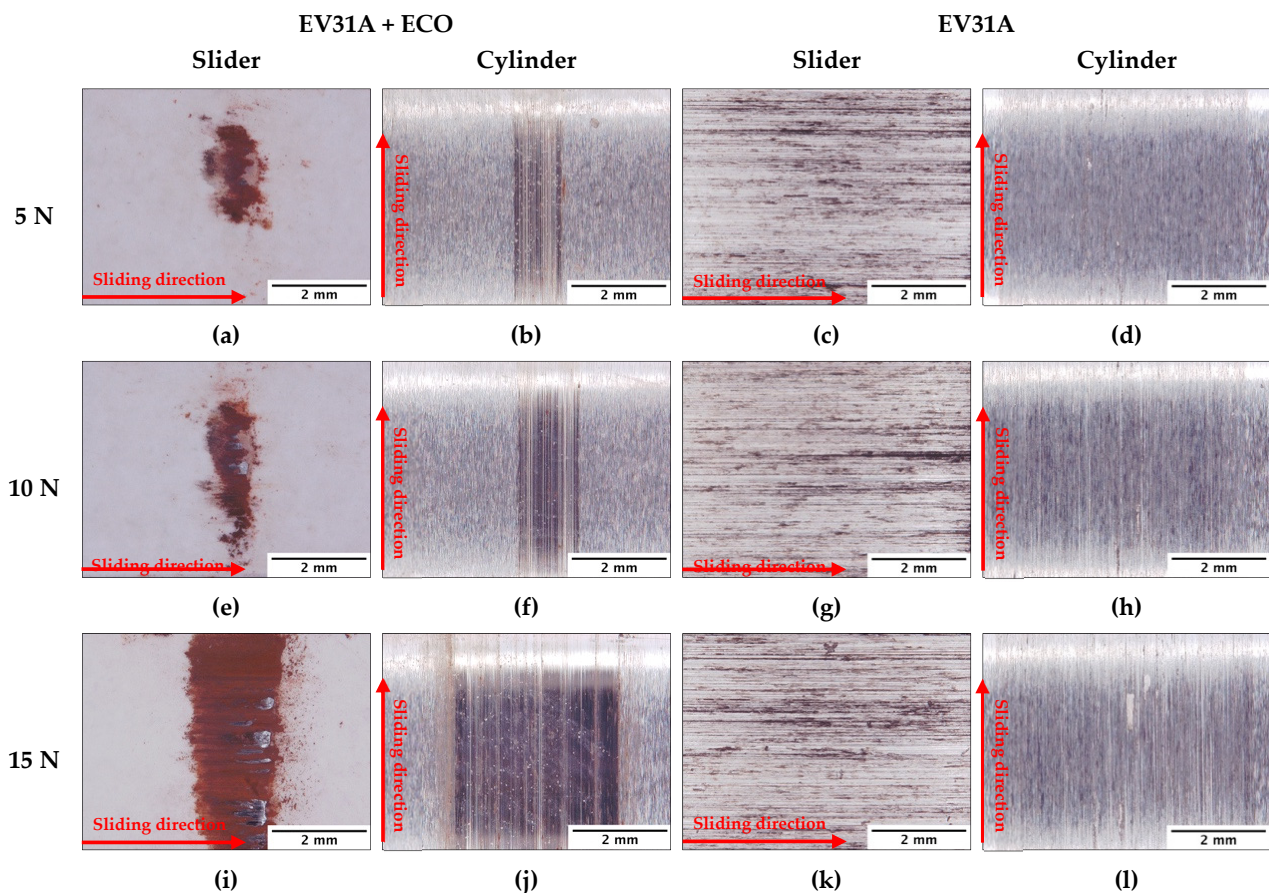


Figure 8. Dry sliding tests (vs. 100Cr6 steel, 1000 m, 0.3 m/s): general view (3D digital microscopy images) of wear scars on both sliders (a,c,e,g,i,k) and cylinder (b,d,f,h,j,l) as a function of normal load. ECO-treated (a,b,e,f,i,j) vs. untreated EV31A-T6 (c,d,g,h,k,l).

For ECO-treated sliders, when the applied load increased to 60 N, a transition appeared in both COF and vertical displacement plots (related to system wear, i.e., wear of both cylinder and slider, Figure 9a). It is worth recalling here that vertical displacement plots show data from the LVDT (Section 2.2): an increasing trend denotes material removal (i.e., wear), while a decreasing trend denotes material deposition (i.e., the formation of transfer layers). More specifically, plots in Figure 9a show that, after about 400 m, the COF measured for coated sliders decreased to comparable values to those measured for untreated EV31A, while the wear rate increased. This friction/wear transition is attributed to the involvement of the substrate in the contact due to the complete consumption of the anodic oxide layer, as wear scars suggest (discussed here below). Hence a maximum load at which the coating still survives the test without any friction and wear transitions was identified, corresponding to the end of the coating life. Above this maximum load (i.e., at 60 N for ECO), a remarkable increase in wear depth was observed (Figure 9b). The maximum load for ECO coating in dry sliding tests (Table 3) was one order of magnitude higher than for PEO layers (50 vs. 5 N) due to the beneficial combination of hardness, thickness, and adhesion of the ECO layer (Table 3).

The average wear depth values measured on sliders (Figure 9b) showed that, even though PEO decreased wear in comparison to the untreated substrate, already at 5 N, the maximum wear depths measured on the PEO layer were comparable to its thickness and the oxide layer was almost completely worn out. The remaining portions of the PEO layer still contributed to support the load and protect the substrate from full involvement in the contact, as demonstrated by the absence of a friction/wear transition in the plots of Figure 7a. Additionally, the SEM observation of worn surfaces showed that both anodic

layers (ECO, Figure 10a and PEO, Figure 10b) limited the occurrence of heavy plastic deformation compared to the untreated alloy (Figure 10c). However, whilst the transfer layer on ECO-treated EV31A consists of fine and partly compacted debris from mild tribo-oxidation of the steel counterpart, the transfer layer on PEO includes many angular fragments due to the onset of fracture in the anodic oxide.

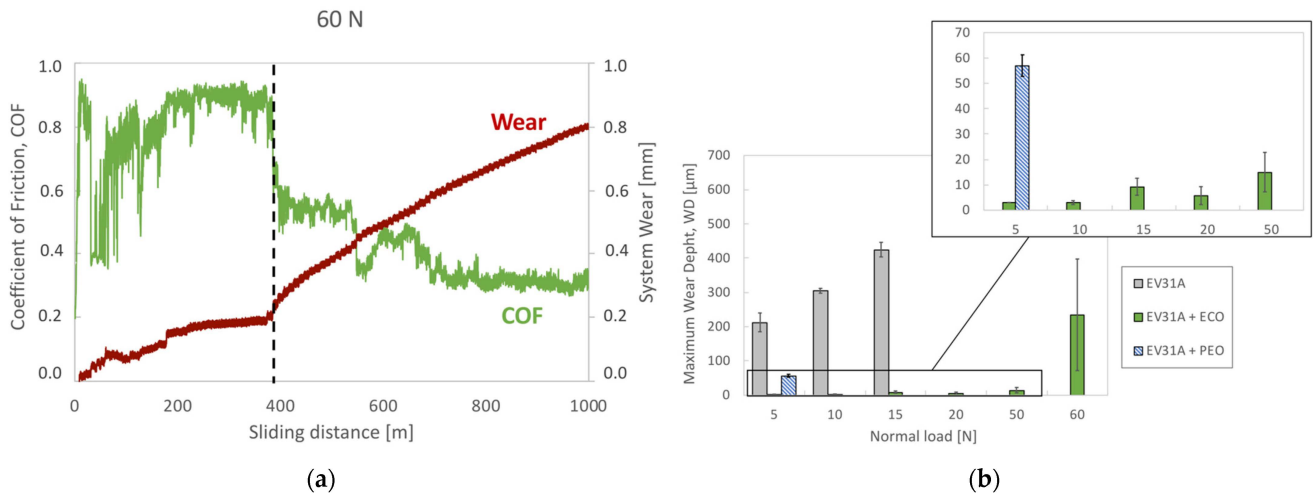


Figure 9. Dry sliding tests (vs. 100Cr6 steel, 1000 m, 0.3 m/s): dynamic coefficient of friction vs. system wear as a function of sliding distance for ECO-treated EV31A at 60 N, showing a transition in the friction and wear behavior (due to involvement of the substrate in the contact, i.e., end of coating life) at about 400 m (a); maximum wear scar depth of sliders measured after dry sliding tests: the inset highlights data for ECO and PEO layers up to 50 N (data for PEO-treated EV31A from [28]) (b).

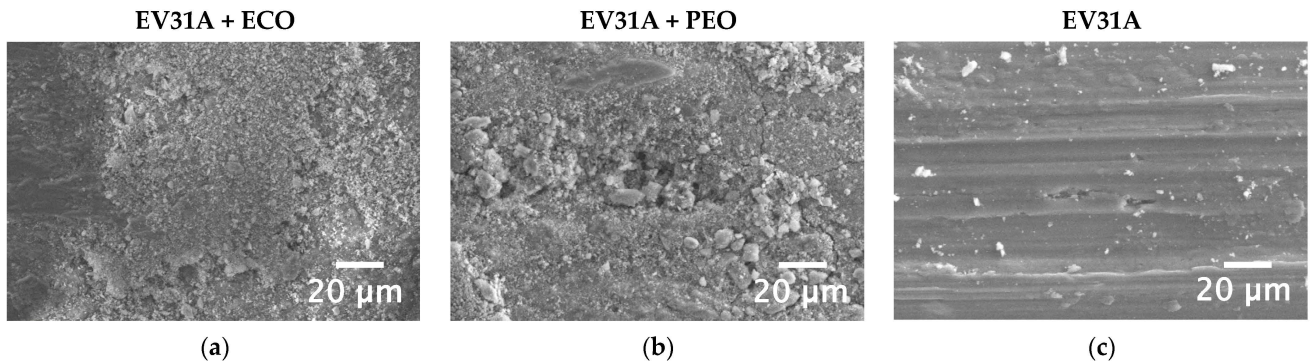


Figure 10. Dry sliding tests (vs. 100Cr6 steel, 5 N, 1000 m, 0.3 m/s): SEM micrographs of wear scars comparing ECO (a) and PEO-treated (b) samples with untreated EV31A-T6 (c).

Conversely, the wear depth on the ECO-treated EV31A remains well below the thickness of the anodized layer in the load range from 5 to 50 N, and the worn surface was covered by the previously discussed iron oxide transfer layer, whose stability may also be accounted for the wear depth trend as a function of load in Figure 9b. The high-magnification observation of wear scars on ECO layers (Figure 11) showed that the transfer layer achieved maximum compactness and hence protective efficiency at 20 N (Figure 11c,d), leading to a slight wear depth decrease. Conversely, at 50 N the protective transfer layer started to be consumed (Figure 11e,f), and the wear depth increased (Figure 9b). At 60 N, the substrate appeared at the center of the wear scar (Figure 11g,h): inside deep grooves and plastically deformed areas, wear debris from the substrate and the anodized layer was detected. Angular fragments due to microcracking of the ECO layer were detected inside these grooves (Figure 11h). Microcrack-driven damage accumulation and coating removal in flakes are typically observed in anodic layers on Mg alloys involved in sliding contacts [48].

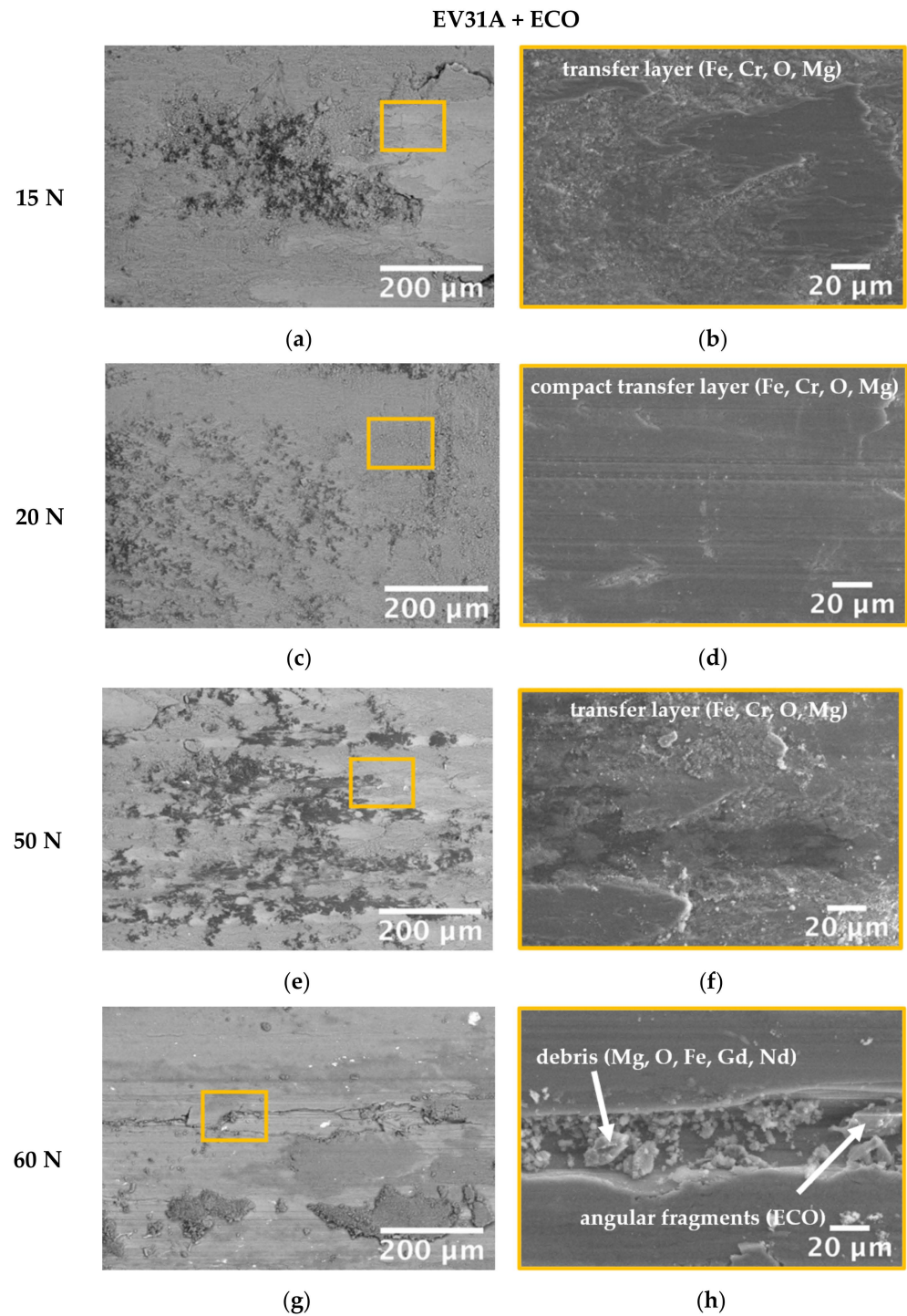


Figure 11. Dry sliding tests (vs. 100Cr6 steel, 1000 m, 0.3 m/s): SEM micrographs of wear scars on ECO-treated sliders at 15 (a,b), 20 (c,d), 50 (e,f) and 60 N (g,h): BSE images (a,c,e,g) and higher magnification SE details (b,d,f,h) in the areas highlighted by the orange frames. The labels indicate the main elements detected by EDS.

3.3. Fatigue Tests

The results of rotating bending fatigue tests, expressed as fatigue strength with a 50% surviving probability according to the staircase method ($\sigma_{D[50\%]}$) for ECO- and PEO-treated EV31A-T6, are reported in Table 3. The fatigue strength at 2×10^6 cycles of the base alloy ranged between 101 ± 12 and 103 ± 17 MPa because surface roughness ranged from 0.3 to $0.8 \mu\text{m}$ [29]. ECO-treated samples showed a fatigue strength comparable to the base alloy

(109 MPa vs. 101–103 MPa); therefore, the ECO treatment did not detrimentally affect the fatigue behavior. The slight differences, especially in terms of standard deviation (5 MPa in the case of ECO and 12 to 17 MPa for the base alloy), can be ascribed to the different stress steps adopted in the experimental campaign (5 MPa and 10 MPa, respectively). However, the PEO treatment reduced the fatigue strength by about 15% compared to the base alloy.

At low magnification (Figure 12), ECO- and PEO-treated samples show comparable fracture surfaces consisting of three distinct regions of fatigue failure: crack nucleation, crack growth, and final failure induced by overloading. A high magnification analysis of the ECO-treated samples is reported in Figures 13–15, which show (i) crack nucleation sites, (ii) crack propagation zone, and (iii) final failure zone, respectively. Corresponding images for PEO-treated samples can be found in [29].

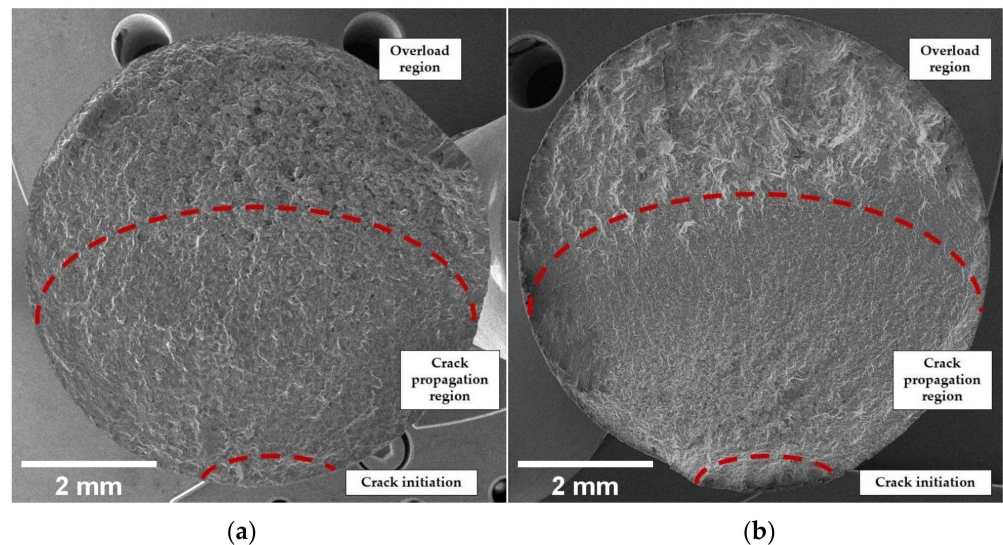


Figure 12. Fatigue tests (4-point rotating bending): SEM overview of the fracture surface of ECO-treated (a) and PEO-treated (b) samples, with distinct regions of fatigue failure.

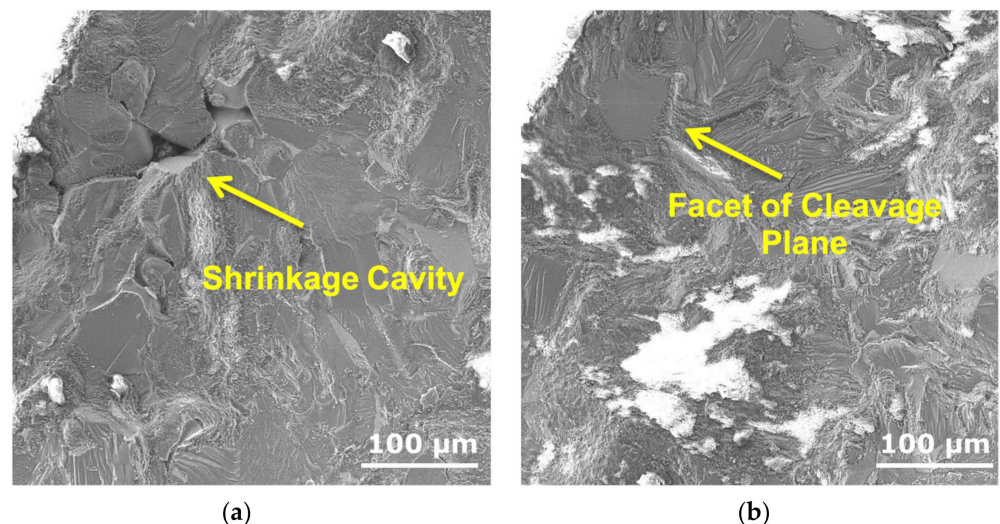


Figure 13. Fatigue tests (4-point rotating bending), fracture surface analysis: SEM images showing crack initiation below the ECO layer-substrate interface at a shrinkage cavity (a) and isolated facet of cleavage plane (b) in ECO-treated EV31A-T6 samples.

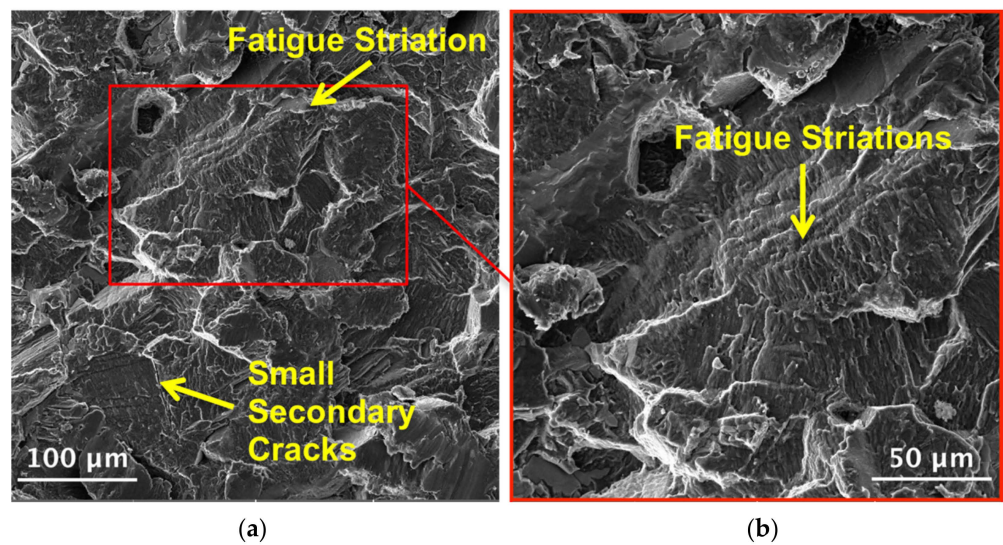


Figure 14. Fatigue tests (4-point rotating bending), fracture surface analysis: SEM images of the crack propagation region showing the typical fatigue striations and small secondary cracks (a,b).

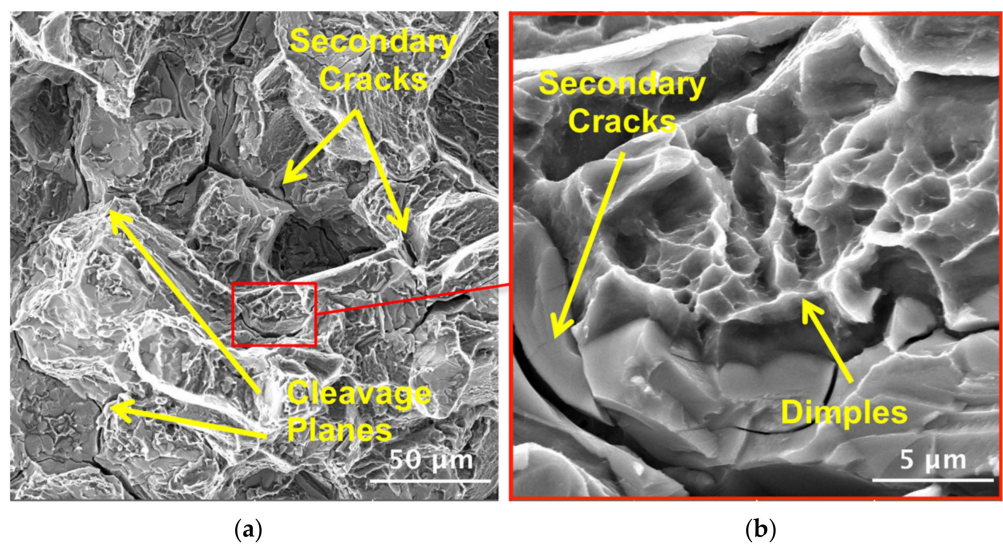


Figure 15. Fatigue tests (4-point rotating bending), fracture surface analysis: SEM images of the overloading region. Intergranular fracture with cleavage planes and secondary cracks (a) and small areas with ultrafine deep dimples (b).

Figure 13 shows that the crack nucleation occurred in the base alloy, slightly below the coating/substrate interface, where the fatigue samples experience the maximum stresses. The nucleation regions were characterized by small shrinkage cavities (Figure 13a) or flat and smooth facets of cleavage planes in correspondence with large grains (Figure 13b). The low number of effective slip systems in the Mg alloys and the high density of dislocations and defects, which increase with increasing grain size, led to the formation of localized damage that propagates fast because of the cyclic loading. Therefore, fatigue crack nucleation was related to features typical of casting Mg alloys similar to those reported in [29,49] and not to defects or decohesion in the anodized layer.

Figure 14 shows images of the crack propagation region, highlighting the presence of the typical fatigue striations. Their formation is generally transgranular, associated with the plastic deformation ahead of the fatigue crack tip induced by twinning mechanisms and dislocations slip. In this region, small secondary transgranular cracks are also clearly visible [50,51].

Finally, the overloading regions (Figure 15) are characterized by an inter-granular fracture mechanism with a brittle morphology, cleavage planes, and secondary cracks, surrounded by small areas with ultrafine deep dimples (Figure 15b), typical of local plastic deformation.

Therefore, in this work, ECO-treated samples underwent fracture due to crack nucleation slightly below the coating/substrate interface, in correspondence with typical microstructural features of the casting Mg alloy [49] acting as the substrate. In particular, small shrinkage cavities and flat and smooth facets of cleavage planes in correspondence with large grains of the substrate were identified (both in ECO-treated EV31A investigated here and in the PEO-treated benchmark [29]) as crack nucleation sites. At the same time, fracture or decohesion of the anodic layers was never observed. Therefore, many factors whose combination may induce the well-documented decrease of fatigue strength in Mg alloys after anodic oxidation may be ruled out in this case. In particular, factors inducing stress concentration, such as defects (primarily cracks) in the anodized layer, the undulation of the alloy/coating interface [40], and corrosion beneath the coating [52] may not be considered responsible for fatigue failure in PEO- and ECO-treated samples investigated in this work. On the other hand, since in PEO samples [29] crack nucleation occurred in the substrate below the interface with the anodic oxide, the generation of a so-called “treatment-affected sub-layer” [20] (TASL) may be considered the leading cause for fatigue failure for PEO-treated EV31A, which experienced a decreased fatigue strength in comparison to the untreated alloy. The accumulation of strain in the TASL, induced by out-of-equilibrium PEO treatment conditions (e.g., rapid fusion and solidification due to intense micro-arc discharges), may lead to tensile residual stresses [53], in turn detrimentally affecting fatigue behavior. Furthermore, it can promote failure initiation at microstructural defects of the EV31A substrate, such as the previously mentioned coarse grains and shrinkage cavities, at lower stress. Conversely, since the ECO treatment operates in a more controlled arc discharge regime than PEO, the formation of a TASL is less likely, and hence the fatigue strength is not detrimentally affected by ECO.

4. Conclusions

This study investigated the influence of ECO coating, produced using an alkaline phosphate-aluminate solution as electrolyte, on dry sliding behavior (block-on-ring contact geometry) and rotating bending fatigue performance of the Rare Earth (RE)-containing Mg alloy EV31A-T6. The results were compared to those obtained in the same testing conditions for untreated and PEO-coated EV31A-T6 alloy and related to microstructural, micro-mechanical, and fractographical analysis. The following conclusions can be drawn:

- Less intense micro arcs generated by the discharge regime in the ECO process resulted in a denser anodized layer than in PEO.
- In dry sliding tests vs. 100Cr6 bearing steel, the ECO-treated alloy showed a critical coating failure load one order of magnitude higher than the PEO-treated alloy.
- At 5 N normal load, the maximum wear depth of the ECO-treated alloy was one order of magnitude higher than for PEO-treated samples. In the same conditions, the coefficient of friction of the ECO-treated alloy was about 40% lower than that of PEO-treated samples.
- With the same surface finish, no decrease in fatigue strength was observed for ECO-treated samples compared to the untreated alloy, while the industrial PEO-treated samples induced a 15% fatigue strength decrease.

The ECO process introduced improvements in tribological behavior and cyclic mechanical performance compared to the PEO process, thanks to the increased compactness and lower defectivity of the anodized layer induced by the minimization of destructive arc discharges during coating growth. Therefore, the ECO process could constitute an optimal solution to improve high-performance Mg alloy components' wear and corrosion resistance.

Author Contributions: Conceptualization, C.M. and P.S.; methodology, G.D.E., C.M. and L.T.; validation, C.M. and L.T.; investigation, I.B. and G.D.E.; data curation, C.M. and A.M.; writing—original draft preparation, G.D.E. and L.T.; writing—review and editing, G.D.E., L.T., C.M. and A.M.; supervision, C.M.; project administration, A.M. and C.M.; funding acquisition, A.M. and C.M. All authors have read and agreed to the published version of the manuscript.

Funding: Funded by the European Union—NextGenerationEU (National Sustainable Mobility Center CN00000023, Italian Ministry of University and Research Decree n. 1033-17/06/2022, Spoke 11—Innovative Materials & Lightweighting). The opinions expressed are only those of the authors and should not be considered representative of the European Union or the European Commission’s official position. Neither the European Union nor the European Commission can be held responsible for them.

Institutional Review Board Statement: Not applicable.

Informed Consent Statement: Not applicable.

Data Availability Statement: Not applicable.

Acknowledgments: The authors thank Simone Messieri at Ducati Motor Holding SpA for the helpful discussion and sample supply and Alessandro Bernardi for his contribution to the experimental work.

Conflicts of Interest: The authors declare no conflict of interest.

References

- Housh, S.; Mikucki, B.; Stevenson, A. Selection and Application of Magnesium and Magnesium Alloys. In *ASM Handbook, Volume 2: Properties and Selection: Nonferrous Alloys and Special-Purpose Materials*; ASM International: Novelty, OH, USA, 1990; pp. 455–479.
- Peng, L.; Fu, P.; Li, Z.; Wang, Y.; Jiang, H. High cycle fatigue properties of cast Mg-xNd-0.2Zn-Zr alloys. *J. Mater. Sci.* **2014**, *49*, 7105–7115. [[CrossRef](#)]
- Pan, F.; Yang, M.; Chen, X. A Review on Casting Magnesium Alloys: Modification of Commercial Alloys and Development of New Alloys. *J. Mater. Sci. Technol.* **2016**, *32*, 1211–1221. [[CrossRef](#)]
- Peng, L.M.; Fu, P.H.; Li, Z.M.; Yue, H.Y.; Li, D.Y.; Wang, Y.X. High cycle fatigue behaviors of low pressure cast Mg-3Nd-0.2Zn-2Zr alloys. *Mater. Sci. Eng. A* **2014**, *611*, 170–176. [[CrossRef](#)]
- Wang, F.; Dong, J.; Jiang, Y.; Ding, W. Cyclic deformation and fatigue of extruded Mg-Gd-Y magnesium alloy. *Mater. Sci. Eng. A* **2013**, *561*, 403–410. [[CrossRef](#)]
- Stanford, N.; Barnett, M. Effect of composition on the texture and deformation behaviour of wrought Mg alloys. *Scr. Mater.* **2008**, *58*, 179–182. [[CrossRef](#)]
- Hadorn, J.P.; Hantzsche, K.; Yi, S.; Bohlen, J.; Letzig, D.; Agnew, S.R. Effects of solute and second-phase particles on the texture of Nd-containing Mg alloys. *Metall. Mater. Trans. A* **2012**, *43*, 1363–1375. [[CrossRef](#)]
- Mirza, F.A.; Chen, D.L.; Li, D.J.; Zeng, X.Q. Effect of rare earth elements on deformation behavior of an extruded Mg-10Gd-3Y-0.5Zr alloy during compression. *Mater. Des.* **2013**, *46*, 411–418. [[CrossRef](#)]
- Wu, G.; Fan, Y.; Gao, H.; Zhai, C.; Zhu, Y.P. The effect of Ca and rare earth elements on the microstructure, mechanical properties and corrosion behavior of AZ91D. *Mater. Sci. Eng. A* **2005**, *408*, 255–263. [[CrossRef](#)]
- Mohedano, M.; Arrabal, R.; Pardo, A.; Paucar, K.; Merino, M.C.; Matykina, E.; Mingo, B.; Garcés, G. Galvanic corrosion of rare earth modified AM50 and AZ91D magnesium alloys coupled to steel and aluminium alloys. *Rev. Metal* **2014**, *50*, e002.
- Riontino, G.; Lussana, D.; Massazza, M.; Barucca, G.; Mengucci, P.; Ferragut, R. Structure evolution of EV31 Mg alloy. *J. Alloys Compd.* **2008**, *463*, 200–206. [[CrossRef](#)]
- Magnesium Alloy Castings. *Sand 2.8Nd-1.4Gd-0.4Zn-0.6Zr (EV31A-T6) Solution and Precipitation Heat Treated, Revision A*; AMS4429; SAE International: Warrendale, PA, USA, 2012.
- Chandra, D.; Chauhan, N.R. Surface protective coatings on Mg alloys—A review. *Mater. Today Proc.* **2021**, *47*, 3819–3822. [[CrossRef](#)]
- Wang, J.; Pang, X.; Jahed, H. Surface protection of Mg alloys in automotive applications: A review. *AIMS Mater. Sci.* **2019**, *6*, 567–600. [[CrossRef](#)]
- Gray, J.E.; Luan, B. Protective coatings on magnesium and its alloys—A critical review. *J. Alloys Compd.* **2002**, *336*, 88–113. [[CrossRef](#)]
- Barati Darband, G.; Aliofkhaezrai, M.; Hamghalam, P.; Valizade, N. Plasma electrolytic oxidation of magnesium and its alloys: Mechanism, properties and applications. *J. Magnes. Alloys* **2017**, *5*, 74–132. [[CrossRef](#)]
- Arrabal, R.; Mohedano, M.; Matykina, E. Electrochemical Surface Treatments for Mg Alloys. In *Encyclopedia of Materials: Metals and Alloys*, 1st ed.; Caballero, F.G., Ed.; Elsevier: Amsterdam, The Netherlands, 2022; pp. 87–112.
- Blawert, C.; Bala Srinivasan, P. 6—Plasma electrolytic oxidation treatment of magnesium alloys. In *Surface Engineering of Light Alloys*, 1st ed.; Dong, H., Ed.; Woodhead Publishing: Cambridge, UK, 2010; pp. 155–183.
- Yerokhin, A.L.; Shatrov, A.; Samsonov, V.; Shashkov, P.; Leyland, A.; Matthews, A. Fatigue properties of Keronite® coatings on a magnesium alloy. *Surf. Coat. Technol.* **2004**, *182*, 78–84. [[CrossRef](#)]

20. Vladimirov, B.V.; Krit, B.L.; Lyudin, V.B.; Morozova, N.V.; Rossiiskaya, A.D.; Suminov, I.V.; Epel'feld, A.V. Microarc oxidation of magnesium alloys: A review. *Surf. Engin. Appl. Electrochem.* **2014**, *50*, 195–232. [[CrossRef](#)]
21. Klein, M.; Lu, X.; Blawert, C.; Kainer, K.U.; Zheludkevich, M.L.; Walther, F. Influence of plasma electrolytic oxidation coatings on fatigue performance of AZ31 Mg alloy. *Corros. Mater.* **2017**, *68*, 50–57. [[CrossRef](#)]
22. Němcová, A.; Skeldon, P.; Thompson, G.E.; Morse, S.; Čížek, J.; Pacal, B. Influence of plasma electrolytic oxidation on fatigue performance of AZ61 magnesium alloy. *Corros. Sci.* **2014**, *82*, 58–66. [[CrossRef](#)]
23. Hussein, R.O.; Northwood, D.O.; Su, J.F.; Nie, X. A study of the interactive effects of hybrid current modes on the tribological properties of a PEO (plasma electrolytic oxidation) coated AM60B Mg-alloy. *Surf. Coat. Technol.* **2013**, *215*, 421–430. [[CrossRef](#)]
24. Saji, V.S. Review of rare-earth-based conversion coatings for magnesium and its alloys. *Mater. Res. Technol.* **2019**, *8*, 5012–5035. [[CrossRef](#)]
25. Liu, C.; Lu, X.; Li, Y.; Chen, Q.; Zhang, T.; Wang, F. Influence of post-treatment process on corrosion and wear properties of PEO coatings on AM50 Mg alloy. *J. Alloys Compd.* **2021**, *870*, 159462. [[CrossRef](#)]
26. Sola, R.; Tonelli, L.; Shashkov, P.; Bogdanoff, T.H.; Martini, C. Anodizing of AA6082-T5 by conventional and innovative treatments: Microstructural characterization and dry sliding behaviour. *Wear* **2020**, *458–459*, 203423. [[CrossRef](#)]
27. De Oliveira, L.A.; dos Santos, S.L.; de Oliveira, V.A.; Antunes, R.A. Influence of Anodization on the Fatigue and Corrosion-Fatigue Behaviors of the AZ31B Magnesium Alloy. *Metals* **2021**, *11*, 1573. [[CrossRef](#)]
28. Tonelli, L.; Pezzato, L.; Dolcet, P.; Dabalà, M.; Martini, C. Effects of graphite nano-particle additions on dry sliding behaviour of plasma-electrolytic-oxidation-treated EV31A magnesium alloy against steel in air. *Wear* **2018**, *404–405*, 122–132. [[CrossRef](#)]
29. Ceschini, L.; Morri, A.; Angelini, V.; Messieri, S. Fatigue Behavior of the Rare Earth Rich EV31A Mg Alloy: Influence of Plasma Electrolytic Oxidation. *Metals* **2017**, *7*, 212. [[CrossRef](#)]
30. International Organization for Standardization. *ISO 1143:2021; Metallic Materials—Rotating Bar Bending Fatigue Testing*. International Organization for Standardization: Geneva, Switzerland, 2021.
31. Angelini, V.; Ceschini, L.; Morri, A.; Apelian, D. Influence of Heat Treatment on Microstructure and Mechanical Properties of Rare Earth-Rich Magnesium Alloy. *Inter. Metalcast.* **2017**, *11*, 382–395. [[CrossRef](#)]
32. *ASTM G77-17; Standard Test Method for Ranking Resistance of Materials to Sliding Wear Using Block-on-Ring Wear Test*. ASTM International: West Conshohocken, PA, USA, 2017.
33. Williams, J.A.; Dwyer-Joyce, R.S. Contact between solid surfaces. In *Modern Tribology Handbook*, 1st ed.; Bhushan, B., Ed.; CRC Press LLC: Boca Raton, FL, USA, 2000; pp. 121–162.
34. Subvol, B. *II-VI and I-VII Compounds; Semimagnetic Compounds*; Madelung, O., Rössler, U., Schulz, M., Eds.; Springer: Berlin/Heidelberg, Germany, 1999; p. 41.
35. International Organization for Standardization. *ISO 12107:2012; Metallic Materials—Fatigue Testing—Statistical Planning and analysis of Data*. International Organization for Standardization: Geneva, Switzerland, 2012.
36. Nie, J.F. Precipitation and Hardening in Magnesium Alloys. *Metall. Mater. Trans. A* **2012**, *43*, 3891–3939. [[CrossRef](#)]
37. Wu, D.; Chen, R.S.; Ke, W. Microstructure and mechanical properties of a sand-cast Mg–Nd–Zn alloy. *Mater. Des.* **2014**, *58*, 324–331. [[CrossRef](#)]
38. ASM International. *ASM Handbook, Metallography and Microstructures*, 1st ed.; George, F., Ed.; Vander Voort ASM International, The Materials Information Society: Materials Park, OH, USA, 2004; Volume 9.
39. Arrabal, R.; Matykina, E.; Hashimoto, T.; Skeldon, P.; Thompson, G.E. Characterization of AC PEO coatings on magnesium alloys. *Surf. Coat. Technol.* **2009**, *203*, 2207–2220. [[CrossRef](#)]
40. Khan, S.A.; Miyashita, Y.; Mutoh, Y.; Koike, T. Effect of anodized layer thickness on fatigue behavior of magnesium alloy. *Mater. Sci. Eng. A* **2008**, *474*, 261–269. [[CrossRef](#)]
41. Monfort, F.; Matykina, E.; Berkani, A.; Skeldon, P.; Thompson, G.E.; Habazaki, H.; Shimizu, K. Species separation during coating growth on aluminium by spark anodizing. *Surf. Coat. Technol.* **2007**, *201*, 8671–8676. [[CrossRef](#)]
42. Matykina, E.; Arrabal, R.; Scurr, D.J.; Baron, A.; Skeldon, P.; Thompson, G.E. Investigation of the mechanism of plasma electrolytic oxidation of aluminium using ¹⁸O tracer. *Corros. Sci.* **2010**, *52*, 1070–1076. [[CrossRef](#)]
43. Durdu, S.; Bayramoğlu, S.; Demirtaş, A.; Usta, M.; Üçışık, A.H. Characterization of AZ31 Mg Alloy coated by plasma electrolytic oxidation. *Vacuum* **2013**, *88*, 130–133. [[CrossRef](#)]
44. International Organization for Standardization. *ISO 20502:2005; Fine Ceramics (Advanced Ceramics, Advanced Technical Ceramics)—Determination of Adhesion of Ceramic Coatings by Scratch Testing*. International Organization for Standardization: Geneva, Switzerland, 2005.
45. Bull, S.J.; Berasetegui, E.G. An overview of the potential of quantitative coating adhesion measurement by scratch testing. *Tribol. Int.* **2006**, *39*, 99–114. [[CrossRef](#)]
46. Srinivasan, P.B.; Liang, J.; Blawert, C.; Dietzel, W. Dry sliding wear behaviour of magnesium oxide and zirconium oxide plasma electrolytic oxidation coated magnesium alloy. *Appl. Surf. Sci.* **2010**, *256*, 3265–3273. [[CrossRef](#)]
47. Rapheal, G.; Kumar, S.; Blawert, C.; Dahotre, N.B. Wear behavior of plasma electrolytic oxidation (PEO) and hybrid coatings of PEO and laser on MRI 230D magnesium alloy. *Wear* **2011**, *271*, 1987–1997. [[CrossRef](#)]
48. Jiang, B.L.; Wang, Y.M. 5—Plasma electrolytic oxidation treatment of aluminium and titanium alloys. In *Surface Engineering of Light Alloys*, 1st ed.; Dong, H., Ed.; Woodhead Publishing: Cambridge, UK, 2010; pp. 110–154.

49. Li, Z.; Wang, Q.; Luo, A.A.; Peng, L.; Zhang, P. Fatigue behavior and life prediction of cast magnesium alloys. *Mater. Sci. Eng. A* **2015**, *647*, 113–126. [[CrossRef](#)]
50. Mirza, F.A.; Chen, D.L.; Li, D.J.; Zeng, X.Q. Cyclic Deformation Behavior of a Rare-Earth Containing Extruded Magnesium Alloy: Effect of Heat Treatment. *Metall. Mater. Trans. A* **2015**, *46*, 1168–1187. [[CrossRef](#)]
51. Li, Z.; Wang, Q.; Luo, A.A.; Fu, P.; Peng, L.; Wang, Y.; Wu, G. High cycle fatigue of cast Mg-3Nd-0.2Zn magnesium alloys. *Metall. Mater. Trans. A* **2013**, *44*, 5202–5215. [[CrossRef](#)]
52. Morri, A.; Ceschini, L.; Martini, C.; Bernardi, A. Influence of Plasma Electrolytic Oxidation on Fatigue Behaviour of ZK60A-T5 Magnesium Alloy. *Coatings* **2020**, *10*, 1180. [[CrossRef](#)]
53. Lonyuk, B.; Apachitei, I.; Duszczyk, J. The effect of oxide coatings on fatigue properties of 7475-T6 aluminium alloy. *Surf. Coat. Technol.* **2007**, *201*, 8688–8694. [[CrossRef](#)]

Disclaimer/Publisher's Note: The statements, opinions and data contained in all publications are solely those of the individual author(s) and contributor(s) and not of MDPI and/or the editor(s). MDPI and/or the editor(s) disclaim responsibility for any injury to people or property resulting from any ideas, methods, instructions or products referred to in the content.